

LETTER TO THE EDITOR

The Tarantula Massive Binary Monitoring

VII. On the nature of the eccentric O+BH binary candidate VFTS 812*

K. Deshmukh^{1,2}, H. Sana^{1,2}, O. Verhamme¹, R. Willcox^{1,2}, P. Marchant³, T. Shenar⁴, F. Backs¹,
 S. Janssens⁵, B. Ludwig¹, L. Mahy⁶, J. O. Sundqvist¹, and J. I. Villaseñor⁷

(Affiliations can be found after the references)

Received; Accepted

ABSTRACT

Massive O-type stars ($M \gtrsim 15 M_{\odot}$) with an X-ray quiet black hole (BH) companion represent a crucial stage in massive binary evolution leading to binary BH mergers. The population of such binaries remains elusive, with $\lesssim 5$ candidate or confirmed systems. The Tarantula nebula harbors thousands of massive stars, 2–3% of which are expected to have BH companions. It is therefore an ideal place to hunt for such systems. Here we analyse 30 epochs of VLT/FLAMES IFU high-resolution observations of the H δ region, as well as archival FLAMES spectroscopy, of VFTS 812, a 17-day single-lined spectroscopic binary with an O4 V primary and a minimum secondary mass of $5.1 M_{\odot}$. Following careful removal of the nebular contamination, spectral disentangling on the new data did not reveal any signature of the hidden companion. We derive $T_{\text{eff}} = 49_{-4}^{+3}$ kK, $\log L = 5.7 \pm 0.1$ and $v_{\text{rot,max}} \sin i = 110_{-35}^{+25}$ km s $^{-1}$ for the O4 V component, yielding a (single star) evolutionary mass of $53_{-5}^{+6} M_{\odot}$ and an age in the range of 0–1.6 Myr. Using injection tests of various luminous artificial companions in our data, we exhaustively rule out the presence of any luminous signature from a main sequence (MS) star more massive than $6 M_{\odot}$. We discuss the possible nature of the companion, suggesting that the rejuvenated O star + BH companion is the most suitable scenario to consistently explain the location, (rejuvenated) young age, eccentricity and lack of companion signature. While this establishes VFTS 812 as a strong candidate O+BH system, follow-up observations are deemed necessary for robust confirmation and to search for accretion signatures on the O4 V star.

Key words. binaries: spectroscopic – stars: black holes – Magellanic Clouds – stars: massive – stars: evolution

1. Introduction

Massive binary evolution is a key formation channel for mergers of neutron stars and black holes (BH) that are detected via gravitational waves. The intermediate OB-type star + BH binary stage holds key evolutionary constraints in this channel. Especially when the OB+BH system has not started to interact, its orbital and dynamical properties retain pristine information in the immediate aftermath of core-collapse of the primary (Vigna-Gómez et al. 2024; Willcox et al. 2025). Around 2–3% of OB stars are predicted to host compact companions (Langer et al. 2020). However, known X-ray quiet OB+BH binaries are scarce, with only a handful recently identified (e.g. Mahy et al. 2022; Shenar et al. 2022a). While the *Gaia* mission is expected to uncover a significant population of OB+BH binaries (Janssens et al. 2022; Nagarajan et al. 2025), spectroscopy will remain the main BH hunting tool for systems with short periods or at large distances such as in the Magellanic Clouds.

VFTS 243 is the only confirmed X-ray quiet OB+BH binary in the Large Magellanic Cloud or LMC (Shenar et al. 2022a), discovered as part of a much broader effort to characterize a sample of 51 O-type single-lined spectroscopic binaries (SB1) in the Tarantula nebula region (Shenar et al. 2022b, referred to as TS22 here onward). A significant fraction of that sample was reclassified as double-lined spectroscopic binaries (SB2) based on spectral disentangling, a technique for the separation of component spectra in spectroscopic binaries (e.g. Hadrava 1995). Others retained their SB1 status or were flagged as uncertain due to

nebular contamination impeding the disentangling process. Subsequently, an improved observational approach was deemed necessary to better identify OB+BH systems in the sample.

VFTS 812, reported as a 17-day eccentric ($e = 0.624$) binary with an O4 V primary weighing about $40 \pm 7 M_{\odot}$ and a minimum secondary mass of $5.1 \pm 0.7 M_{\odot}$, was one such system classified as uncertain (TS22). A BH companion to the O4 V primary would likely descend from a similarly or more massive progenitor, and could potentially be massive itself. Given the minimum secondary mass is in the BH mass regime, we revisit VFTS 812 with new observations aiming to perform better disentangling and establish the nature of its companion. In this letter, we present the observations, data reduction, disentangling analysis and possible nature of the unseen companion.

2. Observations, data reduction and sky subtraction

Prior data for VFTS 812 were obtained with the GIRAFFE spectrograph fed with single FLAMES-MEDUSA fibers on the Very Large Telescope (VLT) in the low resolution modes LR02 and LR03, along with some additional high resolution data around the H α region (Evans et al. 2011; Almeida et al. 2017). In this work, VFTS 812 was observed with the Integral Field Unit (IFU) fiber mode of the FLAMES GIRAFFE spectrograph with the HR03 grating (4032–4203 Å, $R \approx 50000$). This setting was motivated by two expected improvements: (i) a better nebular subtraction compared to single-fiber observations; (ii) higher resolution enabling more robust spectral disentangling.

Between October 2023 and September 2025, a total of 30 epochs were obtained under ESO programs 112.260M and

* Based on observations collected at the European Southern Observatory under ESO program IDs 112.260M and 114.275G (PI: H. Sana).

114.275G (see Appendix A). Raw data were first corrected for cosmic rays using *Astro-SCRAPPY*¹ (van Dokkum 2001). We then used the FLAMES-IFU data reduction recipes within *Esorex* version 3.13.7 to reduce all our data. Each IFU comprises 20 individual fibers bundled in a 4×6 configuration barring the corners, where each fiber (referred to as spaxel here onward) records its own spectrum. Under ideal conditions, four spaxels at the center of the IFU should cover the star, whereas remaining spaxels can be used to obtain the sky background in its immediate vicinity. Poor seeing or IFU misalignment are two main factors that can adversely affect the data quality.

Despite measures taken to improve sky subtraction (see Appendix B), it was non-trivial to choose appropriate star and sky spaxels for perfect subtraction. While there are clear improvements compared to the low resolution single-fiber data, the spatial as well as temporal variability of the nebular line made it challenging to have no residuals after subtraction, and subsequently to obtain spectra appropriate for spectral disentangling. We circumvent this by implementing error spectra in our disentangling approach which can account for imperfect subtraction (see Section 4). A detailed description of our optimal sky subtraction strategy is discussed in Appendix B. In total, spectra for 26 out of 30 epochs were successfully extracted and used for analysis in this work (Table A).

3. Constraining component masses

For an SB1 system with a known mass function, an accurate estimate of the primary mass can place strong constraints on the minimum mass of the secondary. VFTS 812 has a mass function $f = 0.0664 \pm 0.0032 M_{\odot}$ and a primary spectral type of O4 V (TS22). The system does not show eclipses in its light curve, making dynamical masses inaccessible without an astrometric orbit. Previous estimates for VFTS 812 heavily relied on approximate evolutionary masses, with TS22 reporting $M_1 = 40 \pm 7 M_{\odot}$ derived by taking the mean evolutionary mass of all single stars of similar spectral type from the 30 Doradus sample of Schneider et al. (2018). Here, we revisit the primary mass estimates using detailed atmospheric analysis and subsequent constraints on the secondary mass.

3.1. Spectroscopic mass of the primary

We compiled all archival and new FLAMES data for VFTS 812, obtained with the gratings LR02 (397–457 nm), LR03 (450–508 nm), HR03 (403–420 nm) and HR15N (647–679 nm). The spectra from each of the gratings were normalized and coadded in the reference frame of the primary star, clipping out the nebular emission lines before coaddition. We fit FASTWIND atmospheric models (Santolaya-Rey et al. 1997; Sundqvist & Puls 2018) on the combined spectrum to obtain stellar parameters such as effective temperature (T_{eff}), surface gravity ($\log g$) and helium abundance (\bar{Y}_{He}), among others (see full list in Table C.2). The fitting was done with Kiwi-GA, which explores the stellar parameter space allowing for the calculation of statistically derived error margins (Brands et al. 2022, 2025; Verhamme et al. 2024). More details on spectral fitting are discussed in Appendix C.

Because of a lack of He I and nitrogen lines, the derived temperature has large error-margins. The absence of both N V and N IV lines results in only an upper limit on the nitrogen abundance. The derived spectroscopic mass of the star is $34^{+4}_{-7} M_{\odot}$, slightly lower than the evolutionary mass reported in TS22. This

is not fully unexpected as spectroscopic masses are often lower than the derived evolutionary masses (Herrero et al. 1992). This is potentially due to the missing turbulent pressure in spectral codes such as FASTWIND, which can be significant (Moens et al. 2025). Accounting for this turbulence results in an increase in $\log g$, which can increase the mass significantly (González-Torà et al. 2025, Verhamme et al. in prep.). Moens et al. (2025) found a typical velocity corresponding to the turbulent pressure for an O4 V star to be around 50 km s^{-1} . This velocity does not affect the equivalent width of the lines like the micro-turbulent velocity would and is physically more akin to the macro-turbulent velocity. However, this velocity is not used in the broadening of the line profiles in the formal solution. If we include this turbulent pressure in FASTWIND, we find an increased spectroscopic mass of $70^{+20}_{-15} M_{\odot}$, stemming primarily from the increased $\log g$ value while other parameters remain consistent (Table C.2). Since choosing different values will result in significantly different masses, we adopt the parameters derived without including turbulent pressure and turn to evolutionary masses as the more suitable estimate for VFTS 812.

3.2. Evolutionary mass of the primary

With newly performed atmospheric analysis, we obtained an effective temperature $T_{\text{eff}} = 49.2^{+3.0}_{-3.6} \text{ kK}$ and bolometric luminosity $\log(L/L_{\odot}) = 5.72^{+0.07}_{-0.09}$. The primary star was not found to have any significant helium or nitrogen enrichment that could indicate past interactions with the companion. We used the BONNSAI Bayesian tool (Schneider et al. 2014) to fit single star stellar tracks from Brott et al. (2011) to the primary using T_{eff} and $\log(L/L_{\odot})$ as inputs. Surface gravity was not included given its strong dependence on turbulent pressure which is unconstrained.

BONNSAI successfully replicated all observables consistently within $1-\sigma$, although with a low mass tail of high projected rotational velocity solutions. Given the modest $v \sin i$ of $110^{+25}_{-35} \text{ km s}^{-1}$ measured from atmospheric analysis, we excluded all BONNSAI solutions beyond a rotational velocity of 300 km s^{-1} . Subsequently, we constrained the evolutionary mass of the O4 V star to $M_1 = 53.4^{+6.0}_{-5.2} M_{\odot}$, the radius $R_1 = 10.1^{+1.4}_{-0.9} R_{\odot}$, and an estimated age of $0.89^{+0.71}_{-0.84} \text{ Myr}$ (all values are modes). This mass is significantly higher than the corresponding spectroscopic mass ($34^{+4}_{-7} M_{\odot}$). Additionally, the evolutionary mass derived using the $T_{\text{eff}} - \log(L/L_{\odot})$ values with turbulent pressure included is essentially identical ($M_1 = 54.4^{+8.4}_{-5.5} M_{\odot}$).

3.3. Secondary mass and photometric constraints

We combine the orbital parameters of VFTS 812 from TS22 with the mass and radius posterior distributions obtained from BONNSAI to obtain a distribution for the minimum secondary mass which gives $M_{2,\text{min}} > 5.1 M_{\odot}$ at 5% significance. Assuming an isotropic orientation of the orbit, we obtain a secondary mass distribution with $M_2 > 5.3 M_{\odot}$ at 5% significance.

VFTS 812 shows no significant photometric variability or eclipses in OGLE observations (TS22). The absence of eclipses can put an upper limit on the inclination of the binary, assuming that the faint secondary is large enough to eclipse the bright primary. Assuming an MS companion and a mass-radius relation obtained from zero-age main sequence stars in the BONNSAI catalog, we use the absence of a primary eclipse to further constrain the value of M_2 to exceed $5.5 M_{\odot}$ at 5% significance. More on photometric constraints is discussed in Appendix E.

¹ github.com/astropy/astroscrappy

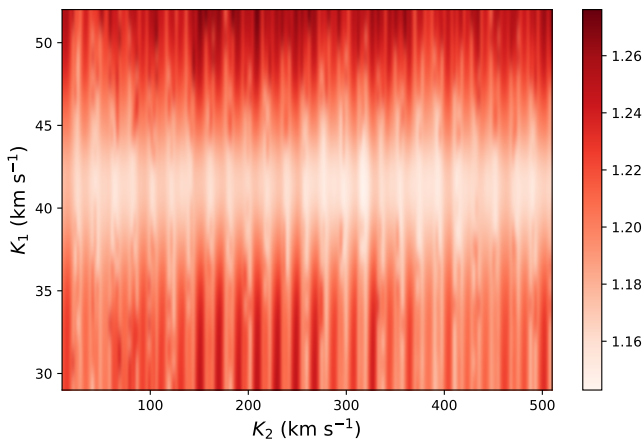


Fig. 1. Reduced chi-squared map from grid disentangling as a function of K_1 (y-axis) and K_2 (x-axis).

4. Spectral disentangling

As discussed in Section 2, the individual epoch spectra of VFTS 812 still have residual features from nebular line subtraction. To minimize the effects of these residuals on the disentangling, we implemented wavelength-dependent error propagation in the shift-and-add technique of [TS22](#)² (see their Section 3.1). We used an error spectrum for each input science spectrum, making it possible to assign negligible weight to the region contaminated by the nebular line. For the HR03 setup, the wavelength region from $4103.9 - 4106.7 \text{ \AA}$ was most affected by the nebular line, and thus essentially excluded from the disentangling process. A mathematical description of our modification to the shift-and-add technique of [TS22](#) is described in Appendix D.

4.1. Searching for a companion

We adopted the orbital solution for VFTS 812 reported by [Almeida et al. \(2017\)](#), with an updated time of periastron passage derived from new observations (Table D.1). Taking an agnostic approach, we performed two-component disentangling over a grid of component radial velocity semi-amplitudes K_1, K_2 ranging from $30 - 52 \text{ km s}^{-1}$ in steps of 1 km s^{-1} and $10 - 500 \text{ km s}^{-1}$ in steps of 2.5 km s^{-1} , respectively. This ensured a thorough exploration of different mass ratios. Figure 1 shows a 2-D chi-squared map of our disentangling analysis. The primary semi-amplitude K_1 was recovered at $41.9 \pm 1.0 \text{ km s}^{-1}$, consistent with $42.7 \pm 0.6 \text{ km s}^{-1}$ reported in [TS22](#). K_2 , however, was unconstrained as evident from the chi-squared map. The disentangled spectrum of the primary is consistent with the O4 V primary, while that for the secondary is essentially flat and featureless (Fig. 2). The latter translates to an absence of a detectable companion, either because it is too faint or dark. To further investigate which companion types can avoid detection in our spectra, we carried out an injection study, as described in the following subsection.

4.2. Limits on the flux and mass of the secondary

To test our ability of detecting companions of different masses, we performed an injection study wherein we injected companion model spectra into the data and attempted to retrieve them with spectral disentangling. Given the O4 V primary and assum-

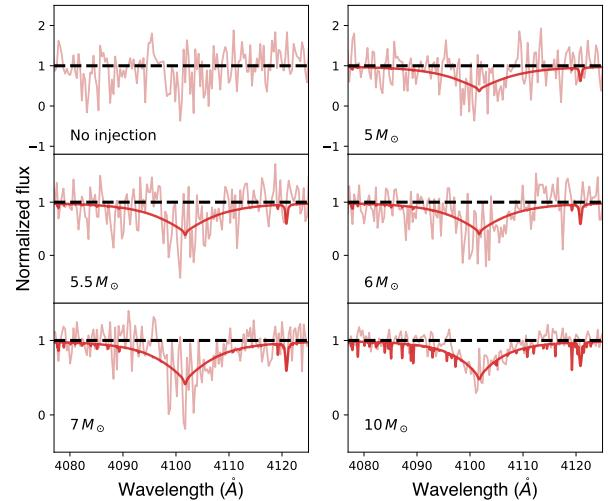


Fig. 2. Disentangled secondary spectra (light red) from the no-injection case (first panel) and different mock datasets (remaining panels) along with labels showing masses of the injected models. Also shown are the injected model spectra (dark red) and the best fit flat line (black). The disentangled spectra are binned by a factor of 3 for better visualization.

ing the secondary is an MS star, we used BONNSAI to determine the radius, temperature and luminosity of the injected companion by fixing its age to that of the primary. We computed FASTWIND model spectra based on these inputs, and convolved them with the Bessel B filter to estimate their flux contribution (Table D.2). Subsequently, we synthesized mock spectra by injecting an MS secondary in the data using the computed flux contribution and with an RV semi-amplitude corresponding to its mass. Mock datasets were made for MS companions of $5, 5.5, 6, 6.5, 7, 8$ and $10 M_\odot$. For every dataset, we ran a companion search using disentangling. The disentangled secondary spectrum was retrieved at the same K_2 value that it was injected at, while keeping the K_1 grid same as Section 4.1. Since the real K_2 is not known, we retrieved the secondary spectrum at different K_2 values for the no-injection case to search for spectral features.

The results for select cases are summarized in Figure 2, along with the companion search run from Section 4.1 with no injected secondary. Each panel shows the disentangled secondary compared with the injected model (flat for the no-injection case). We performed an F -test in the $4072 - 4130 \text{ \AA}$ range to determine whether the model is a better fit to the retrieved spectrum than a featureless flat line, for which we used a 5% significance threshold. The continuum region was determined outside the $4090 - 4112 \text{ \AA}$ region and fixed for both the flat line and model fits. Subsequently, chi-squared values were evaluated in the full $4072 - 4130 \text{ \AA}$ range to compare the fits.

Assuming rotational velocities of $0, 250$ and 500 km s^{-1} for the injected models, we are able to successfully retrieve companions with masses $6 M_\odot$ and above. For the no-injection case, the flat line vs model fits are statistically indistinguishable when tested with $5, 5.5$ and $6 M_\odot$ models. We can therefore confidently rule out a $\gtrsim 6 M_\odot$ luminous MS companion.

5. Discussion and conclusion

Based on our disentangling analysis, we discuss here the potential nature of the system and prospects to establish or reject VFTS 812 as an O+BH binary. We obtain a detection threshold of $6 M_\odot$ for MS companions, with lower mass companions

² github.com/TomerShenar/Disentangling_Shift_And_Add

avoiding detection. The orbital constraint on the other hand implies $M_{2,\min} > 5.1 M_{\odot}$ at 5% significance. Subsequently, we consider a few possible scenarios:

MS companion: It is possible that the companion is an MS star with a mass between 5.1 and $6 M_{\odot}$, which satisfies the orbital constraint yet remains elusive. We are limited by current observations in testing the presence of such a companion. However, in the scenario where VFTS 812 is formed by two young MS stars, its location in 30 Dor remains intriguing: VFTS 812 is offset by $\sim 4.9'$ from R136, the star forming region compatible with the age of VFTS 812 in the 30 Dor complex (Schneider et al. 2018). VFTS 812 is also noticeably isolated; the few stars in its neighborhood are much older B-type stars (Schneider et al. 2018). Furthermore, it shows no indication of a runaway motion, whether in its systemic radial velocity (Sana et al. 2022), or in its *Gaia* proper motion (Stoop et al. 2024), invalidating a scenario where it has been dynamically ejected from R136.

Hot stripped companion: A hot stripped companion formed via binary mass transfer with $M_2 \gtrsim 5.1 M_{\odot}$ peaks in the ultraviolet (UV) regime and is considerably smaller in radius compared to similar-mass MS stars. It thus contributes even less in optical wavelengths in comparison. An excess flux in the ultraviolet (UV) is an effective way to detect stripped companions (Ludwig et al. 2025); however, the UV excess contribution of a $\gtrsim 5.1 M_{\odot}$ stripped star is expected to vanish next to a $53.7 M_{\odot}$ MS companion (see Section S2.1 in Drout et al. 2023). The photometric AB-magnitude colors of VFTS 812 using *Swift* and Bessel filters: $UVM2 - V = 0.78$, $UVW1 - B = 0.64$, $U - V = 0.01$ are all far from passing the UV excess criteria of Ludwig et al. (2025). For companions with $M_2 \gtrsim 11 M_{\odot}$ where stripped stars transition to the Wolf-Rayet regime (Shenar et al. 2019), the companion would be much more luminous and detectable. On the other hand, for $5.1 M_{\odot} \lesssim M_2 \lesssim 11 M_{\odot}$, factors such as an extreme mass ratio, high eccentricity, no evidence of high rotational velocity and He or N enrichment in the primary pose significant challenges for this scenario. We therefore consider the presence of a hot stripped companion unlikely.

Compact companion: If the companion is a compact object, the orbital constraint on M_2 essentially requires a BH companion. A significant kick during BH formation could explain its isolated location and eccentricity (Mahy et al. 2022; Willcox et al. 2025). Although the primary lacks obvious signatures of past interaction, if we consider that it was rejuvenated via accretion followed by BH formation with a kick, we can explain its young age, isolated location and eccentricity.

Fast rotating primary: In Section 3.2, we excluded high rotational velocity ($> 300 \text{ km s}^{-1}$) solutions for the primary star from BONNSAI. If the primary was a fast rotator, the following can be said about potential companions: (i) For an MS or stripped companion with the primary rotational axis and the orbital axis aligned, the orbital inclination would be $i \lesssim 20^\circ$. This would imply a significantly higher minimum companion mass, favoring its detection. (ii) For a BH companion, a BH formation kick could disturb the above alignment and similar constraints on its mass cannot be made, although the remaining arguments made earlier about a BH companion would still apply.

Given these formation scenario challenges, VFTS 812 remains a compelling testbed for binary evolution models. The major limitation of our data is the S/N, which holds the key to confirm the presence or absence of a luminous companion. We encourage follow-up high-S/N spectroscopic observations to confirm the nature of the unseen companion in VFTS 812. Complementary far-ultraviolet spectroscopy can also greatly assist in determining accurate atmospheric parameters of the primary.

Acknowledgements. This research received support from the Flemish Government under the long-term structural Methusalem funding program, project SOUL: Stellar evolution in full glory, grant METH/24/012 at KU Leuven. SJ acknowledges support from the Japan Society for the Promotion of Science (JSPS) as a postdoctoral fellow. JIV acknowledges support from the European Research Council for the ERC Advanced Grant 101054731. TS acknowledges support from the Israel Science Foundation (ISF) under grant number 0603225041 and from the European Research Council (ERC) under the European Union’s Horizon 2020 research and innovation program (grant agreement 101164755/METAL).

References

Abdul-Masih, M., Sana, H., Sundqvist, J., et al. 2019, *ApJ*, 880, 115
 Almeida, L. A., Sana, H., Taylor, W., et al. 2017, *A&A*, 598, A84
 Asplund, M., Grevesse, N., Sauval, A. J., & Scott, P. 2009, *ARA&A*, 47, 481
 Brands, S. A., Backs, F., de Koter, A., et al. 2025, *A&A*, 697, A54
 Brands, S. A., de Koter, A., Bestenlehner, J. M., et al. 2022, *A&A*, 663, A36
 Brott, I., de Mink, S. E., Cantiello, M., et al. 2011, *A&A*, 530, A115
 Debnath, D., Sundqvist, J. O., Moens, N., et al. 2024, *A&A*, 684, A177
 Drout, M. R., Götzberg, Y., Ludwig, B. A., et al. 2023, *Science*, 382, 1287
 Evans, C. J., Taylor, W. D., Hénault-Brunet, V., et al. 2011, *A&A*, 530, A108
 Fabry, M., Hawcroft, C., Mahy, L., et al. 2021
 Fitzpatrick, E. L. 1999, *PASP*, 111, 63
 González-Torà, G., Sander, A. A. C., Sundqvist, J. O., et al. 2025, *A&A*, 694, A269
 Hadrava, P. 1995, *A&AS*, 114, 393
 Hawcroft, C., Sana, H., Mahy, L., et al. 2021, *A&A*, 655, A67
 Herrero, A., Kudritzki, R. P., Vilchez, J. M., et al. 1992, The mass and helium discrepancy in massive young stars, ed. U. Heber & C. S. Jeffery, Vol. 401, 21
 Janssens, S., Shenar, T., Sana, H., et al. 2022, *A&A*, 658, A129
 Langer, N., Schürmann, C., Stoll, K., et al. 2020, *A&A*, 638, A39
 Ludwig, B., Drout, M. R., Gotberg, Y., Lang, D., & Laroche, A. 2025, *ApJ*, in press
 Mahy, L., Sana, H., Shenar, T., et al. 2022, *A&A*, 664, A159
 Moens, N., Debnath, D., Verhamme, O., et al. 2025, *A&A*, 704, A121
 Mokiem, M. R., de Koter, A., Puls, J., et al. 2005, *A&A*, 441, 711
 Nagarajan, P., El-Badry, K., Chawla, C., et al. 2025, *PASP*, 137, 044202
 Pietrzyński, G., Graczyk, D., Gallenne, A., et al. 2019, *Nature*, 567, 200
 Puls, J., Urbaneja, M. A., Venero, R., et al. 2005, *A&A*, 435, 669
 Sana, H., de Koter, A., de Mink, S. E., et al. 2013, *A&A*, 550, A107
 Sana, H., Ramírez-Agudelo, O. H., Hénault-Brunet, V., et al. 2022, *A&A*, 668, L5
 Santolaya-Rey, A. E., Puls, J., & Herrero, A. 1997, *A&A*, 323, 488
 Schneider, F. R. N., Langer, N., de Koter, A., et al. 2014, *A&A*, 570, A66
 Schneider, F. R. N., Ramírez-Agudelo, O. H., Tramper, F., et al. 2018, *A&A*, 618, A73
 Shenar, T., Sablowski, D. P., Hainich, R., et al. 2019, *A&A*, 627, A151
 Shenar, T., Sana, H., Mahy, L., et al. 2022a, *Nature Astronomy*, 6, 1085
 Shenar, T., Sana, H., Mahy, L., et al. 2022b, *A&A*, 665, A148
 Stoop, M., de Koter, A., Kaper, L., et al. 2024, *Nature*, 634, 809
 Sundqvist, J. O. & Puls, J. 2018, *A&A*, 619, A59
 Tramper, F., Sana, H., de Koter, A., Kaper, L., & Ramírez-Agudelo, O. H. 2014, *A&A*, 572, A36
 van Dokkum, P. G. 2001, *PASP*, 113, 1420
 Verhamme, O., Sundqvist, J., de Koter, A., et al. 2024, *A&A*, 692, A91
 Vigna-Gómez, A., Willcox, R., Tamborra, I., et al. 2024, *Phys. Rev. Lett.*, 132, 191403
 Willcox, R., Marchant, P., Vigna-Gómez, A., et al. 2025, *A&A*, 700, A59

¹ Institute of Astronomy, KU Leuven, Celestijnlaan 200D, 3001 Leuven, Belgium

e-mail: kunalprashant.deshmukh@kuleuven.be

² Leuven Gravity Institute, KU Leuven, Celestijnlaan 200D, box 2415 3001 Leuven, Belgium

³ Sterrenkundig Observatorium, Universiteit Gent, Krijgslaan 281 S9, B-9000 Gent, Belgium

⁴ The School of Physics and Astronomy, Tel Aviv University, Tel Aviv 6997801, Israel

⁵ Research Center for the Early Universe, Graduate School of Science, The University of Tokyo, 7-3-1 Hongo, Bunkyo-ku, Tokyo 113-0033, Japan

⁶ Royal Observatory of Belgium, B-1180 Brussels, Belgium

⁷ Max-Planck-Institut für Astronomie, Königstuhl 17, D-69117 Heidelberg, Germany

Appendix A: Summary of observations

Table A.1. FLAMES/IFU observation summary for VFTS 812.

Epoch #	MJD _{start}	Grade	S/N
1	60219.28064	C	28.5
2	60270.16428	D	43.2
3	60296.04246	C	14.1
4	60313.07963	C	41.0
5	60320.15121	C	13.6
6	60343.12974	C	28.2
7*	60356.04970	C	—
8	60356.05376	C	27.1
9	60376.03744	A	27.6
10*	60379.02918	A	—
11	60386.02954	A	22.5
12	60388.04696	A	40.4
13*	60390.03915	A	—
14	60585.31163	A	19.4
15	60608.21356	A	46.4
16	60644.21282	A	25.2
17	60647.21363	A	48.1
18	60666.18454	A	43.6
19	60674.21820	A	49.8
20	60678.05188	A	31.0
21	60680.07364	A	21.2
22	60683.22568	A	23.8
23	60697.17431	A	36.6
24	60707.11384	C	26.2
25	60709.08383	A	16.2
26*	60740.10798	B	—
27	60765.00890	C	10.7
28	60768.98720	B	20.5
29	60933.35310	A	18.6
30	60947.26876	C	43.3

Notes: For every epoch, we provide the MJD at the start of the observation (column 2), grade assigned by ESO (column 3), and S/N measured in the continuum region between 4050 – 4060 Å (column 4). For epochs marked with an asterisk, the data quality was too poor to extract spectra.

Appendix B: Optimal sky subtraction

The spatial and temporal variation in the Tarantula nebula makes it difficult to obtain perfect sky subtraction. The IFU approach is helpful to remedy this by capturing the sky background in the vicinity of the star for every epoch. However, we noticed two important features in our observations: (i) The star is not always aligned on the central four spaxels and changes positions on the IFU from epoch to epoch (Fig. B.1); and (ii) The nebular emission in the immediate vicinity of the star is not always identical to that in the star itself (Fig. B.2). Perfect sky subtraction is thus not guaranteed even with IFU observations. This was considered when choosing the spaxels for the star and sky regions. Here, we discuss two approaches along with their suitability for spectral disentangling.

In the first approach, we prioritized perfect nebular subtraction to leverage the capabilities of the IFU mode. For each epoch, we selected the four brightest spaxels for the star and summed them up. To obtain perfect subtraction, we tried different combinations of four other spaxels to sum up and find a suitable sky spectrum. This was done for each epoch individually, leading to varying choices for sky spaxels across epochs. In many cases, we chose sky spaxels immediately next to the star spaxels for the best possible subtraction. This came at the cost of subtracting some of the star signal present in these spaxels, re-

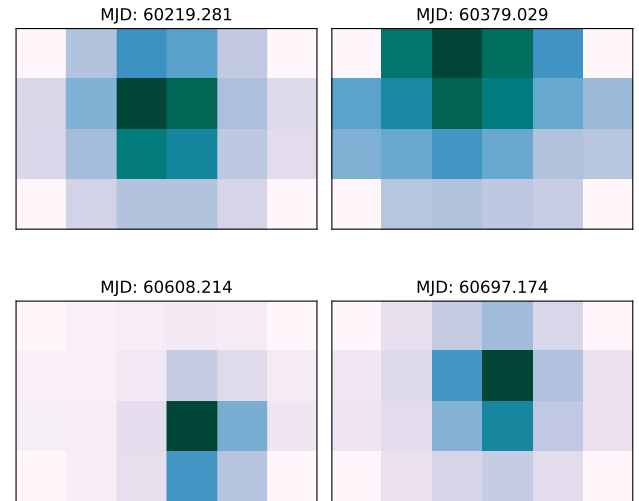


Fig. B.1. Four examples of IFU data shown with their Modified Julian Dates (MJDs) at start of observation. In every panel, the 20 spaxels barring the corners are scaled with their median flux, with light colors representing low and dark representing high flux. The position and point spread function of the star can be seen varying across the four epochs.

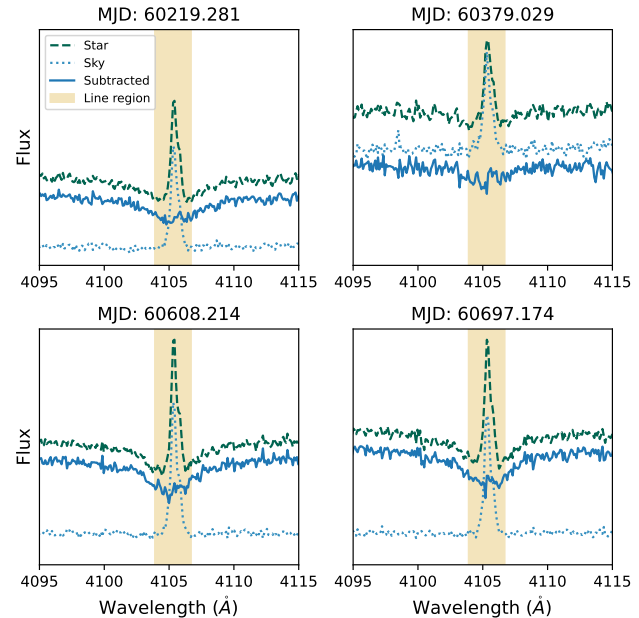


Fig. B.2. For the same four examples as Figure B.1, we show spectra for the star spaxels (dashed), sky spaxels (dotted) and the resulting sky-subtracted spectrum (solid). Also highlighted is the “line region” (yellow) from 4103.9–4106.7 Å that was most affected by nebular contamination. The sky-subtracted spectra in the line region clearly show variable residual features across the four epochs.

ducing the signal-to-noise ratio (S/N) of the resulting spectrum. Despite these considerations, the nebular subtraction in many spectra remained imperfect and variable across epochs as seen in Figure B.2. This can severely hamper spectral disentangling when dealing with faint/unseen companions that require the best quality data to obtain meaningful constraints. Furthermore, the compromise on S/N is yet another factor making disentangling more challenging.

In the second approach, given that the nebular subtraction leaving small residuals was inevitable, we prioritized S/N which

is particularly important when searching for a faint companion. We followed the same procedure as before to select the four star spaxels. However, for the sky subtraction, we chose four spaxels farthest from the star that were unlikely to have any significant signal from the star. This resulted in a more accurate sky subtraction for the continuum region, while the nebular subtraction was slightly compromised. To further optimize the process, we took advantage of the fact that the sky background did not have any spectral lines in our wavelength range other than the H_{δ} nebular emission line. We divided the sky spectrum into two parts: the H_{δ} line spanning the small wavelength range of $4103.9 - 4106.7 \text{ \AA}$, and the continuum region covering the remaining wavelength range. The latter was modeled with a cubic polynomial and combined with actual data within the H_{δ} line to form a new sky spectrum. The main motivation behind doing this was to avoid adding extra continuum noise in the final sky subtracted spectra. Although the nebular subtraction in this case slightly worsened compared to the previous approach, it is circumvented successfully in our modified disentangling method discussed in Section 4.

Appendix C: Atmospheric analysis

We use FASTWIND (Santolaya-Rey et al. 1997; Sundqvist & Puls 2018) and Kiwi-GA (Brands et al. 2022, 2025) to fit the spectral lines of VFTS 812. This method is an evolution from previous genetic algorithm based fitting solutions (Mokiem et al. 2005; Tramper et al. 2014; Abdul-Masih et al. 2019; Hawcroft et al. 2021). We allow for 6 fit parameters (T_{eff} , $\log_{10} g$, \dot{M} , $n_{\text{He}}/n_{\text{H}}$, $v_{\text{rot,max}} \sin i$, and nitrogen abundance). Here $v_{\text{rot,max}} \sin i$ is the only broadening mechanism included meaning this value could be read as the combination of macro turbulence and rotational broadening. The micro turbulence is kept fixed at 10 km s^{-1} . The nitrogen number abundance N is expressed in $\epsilon_N = 12 + \log_{10}(n_N/n_{\text{H}})$. We used FASTWIND version 10.5 (Puls et al. 2005) with metallicity scaled to 0.5 times the solar metallicity (Asplund et al. 2009) and a smooth wind. In total we have access to 17 spectral windows (Figure C.1) containing a total of 41 diagnostic spectral lines (Table C.1). In this method all lines were fitted at the same time and the total goodness of fit was taken into account to decide the quality of the fit. This means that even lines which are generally not thought to be indicative lines of a parameter still contribute to the determination of that parameter. To determine the radius of the star, we used the observed K-band magnitude of 14.17, an estimated 50 kpc distance to the LMC (Pietrzyński et al. 2019), and the $R_V = 3.1$ extinction law Fitzpatrick (1999) to scale the radius such that the model spectral energy distribution crosses the K-band luminosity. Table C.2 lists the best fit values with their $1-\sigma$ uncertainty.

When using the unaltered version of FASTWIND, turbulent pressure is not included into the calculation of the stellar structure. Debnath et al. (2024) showed that the 2D average stellar structure is very different from the 1D models used for spectral synthesis. Additionally, they showed that by including turbulent pressure in the hydrostatic equation, it is possible to offset this difference. Moens et al. (2025) showed through a grid of multi-D models that the turbulent pressure is highly dependent on the Eddington factor of the star, giving us an indication of which turbulent pressure to include. Subsequently, the derived surface gravity, and the spectroscopic mass goes up as the turbulent pressure increases (González-Torà et al. 2025, Verhamme et al. in prep). All this led us to try a spectral fit in which we included a constant turbulent velocity of 50 km s^{-1} . The results of this fit did not change any parameters outside of the error-margins besides from

Table C.1. List of all spectral lines which are fitted.

Ion	Rest wavelength [Å]	Line window
He II	4025.4	He II 4026
He I	4026.2	He II 4026
N IV	4057.8	N IV 4058
S IV	4088.9, 4116.1	H_{δ}
N III	4097.4, 4103.4	H_{δ}
H I	4101.7	H_{δ}
He I	4143.8	He I 4143
N III	4195.8, 4200.1, 4215.77	He II 4200
He II	4199.6	He II 4200
He II	4338.7	H_{γ}
H I	4340.5	H_{γ}
O II	4317.1, 4319.6, 4366.9	H_{γ}
N III	4345.7, 4332.91	H_{γ}
He I	4387.9	He I 4387
He I	4471.5	He I 4471
N III	4534.6	He II 4541
He II	4541.4	He II 4541
N V	4603.7	N V 4603
He II	4685.6	He II 4686
He I	4713.1	He I 4713
N III	4858.7, 4859.0, 4861.3, 4867.1, 4867.2, 4873.6	$H\beta$
He II	4859.1	$H\beta$
H I	4861.4	$H\beta$
He I	4921.9	He I 4922
He II	6527.1	He II 6527
He II	6559.8	$H\alpha$
H I	6562.8	$H\alpha$
He I	6678.2	He II 6683
He II	6682.8	He II 6683

Notes: The first column shows the atom and its ionization stage which is responsible for the transition. The second column shows the corresponding rest wavelength with possible multiplets. The third column shows where to find this line in the fit summary (Fig. C.1).

the surface gravity and thus the resulting derived spectroscopic mass. The results of this fit are also given in Table C.2 next to the normal fit for ease of comparison. Figure C.1 shows the best fit models with and without turbulent pressure, compared to the data with the $1-\sigma$ range of the spectra. The spectroscopic mass strongly depends on the chosen turbulent velocity, which is only loosely bound by the radiation hydrodynamical models (Moens et al. 2025). Because it is not possible to constrain the turbulent velocity observationally, strong constraints on spectroscopic mass are inaccessible for VFTS 812.

Appendix D: Spectral disentangling

A comprehensive description of the shift-and-technique is provided in Section 3.1 of TS22. Making an agnostic assumption about the binary being an SB2, a 2-dimensional grid disentangling can be used to constrain the respective RV semi-amplitudes K_1 and K_2 of the primary and secondary components. A chi-squared minimization can yield the best (K_1, K_2) combination, where the chi-squared is calculated as

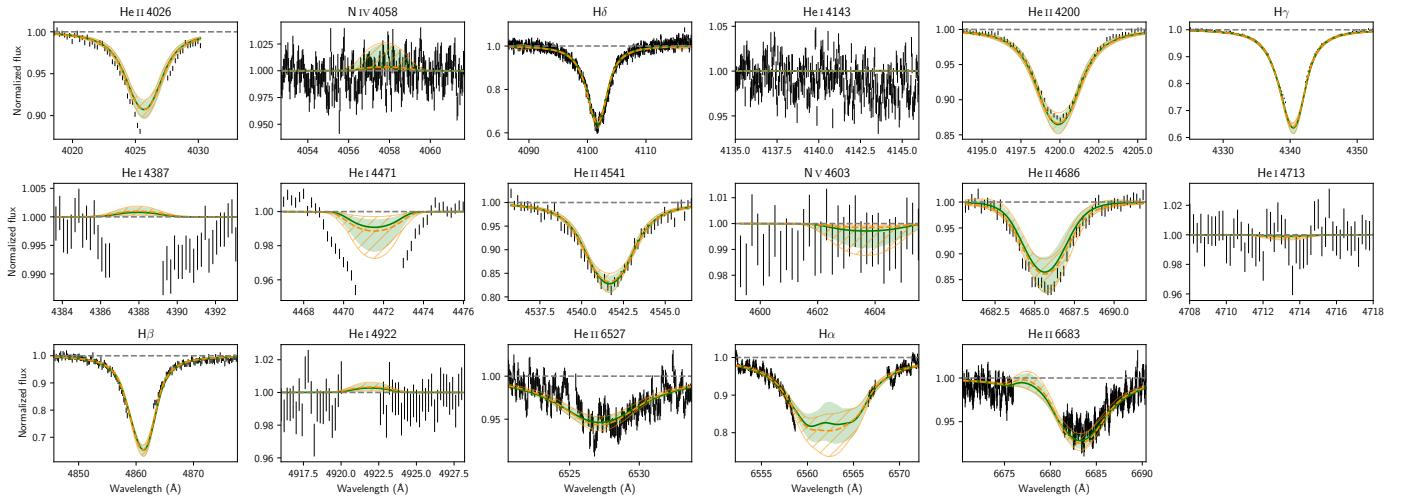


Fig. C.1. Spectral fit of VFTS 812. Data is shown in black; the dark green line denotes the best fit and the light green region the $1-\sigma$ uncertainty region of the fit without turbulent pressure. The dashed orange line and the hatched orange area show the best fit and $1-\sigma$ uncertainty of the fit with turbulence.

Table C.2. Spectral fit values with $1-\sigma$ uncertainty.

Parameter	without v_{turb}	with v_{turb}
$T_{\text{eff}} [\text{kK}]$	$49.2^{+3.0}_{-3.6}$	$47.6^{+5.2}_{-3.0}$
$\log_{10} g [\text{cm/s}^2]$	$3.96^{+0.08}_{-0.10}$	$4.26^{+0.16}_{-0.12}$
$\log_{10}(\dot{M}) [\text{M}_\odot/\text{yr}]$	$-6.50^{+0.10}_{-0.15}$	$-6.55^{+0.10}_{-0.20}$
$Y_{\text{He}} [n_{\text{He}}/n_{\text{H}}]$	$0.10^{+0.02}_{-0.03}$	$0.09^{+0.02}_{-0.02}$
$v_{\text{rot,max}} \sin i [\text{km s}^{-1}]$	110^{+25}_{-35}	120^{+25}_{-35}
$N[12 + \log_{10}(n_{\text{N}}/n_{\text{H}})]$	$5.85^{+0.90}_{-1.05}$	$5.80^{+1.05}_{-1.05}$
$\log L [\text{L}_\odot]$	$5.72^{+0.07}_{-0.09}$	$5.68^{+0.13}_{-0.08}$
$R [\text{R}_\odot]$	$10.08^{+0.39}_{-0.30}$	$10.26^{+0.34}_{-0.54}$
$M_{\text{spec}} [\text{M}_\odot]$	34^{+5}_{-4}	70^{+20}_{-15}

$$\chi^2(K_1, K_2) = \frac{1}{N_\lambda(N_{\text{epochs}} - 2)} \sum_{i=1}^{N_{\text{epochs}}} \sum_{k=1}^{N_\lambda} \frac{(A_{i,k} + B_{i,k} - O_{i,k})^2}{\sigma_i^2}. \quad (\text{D.1})$$

Here, N_{epochs} is the number of epochs, N_λ is the number of wavelength bins in the selected range of the spectrum, $A_{i,k}$ and $B_{i,k}$ are disentangled spectra and $O_{i,k}$ is the observed spectrum at wavelength λ_k . The noise term, σ_i is calculated in the continuum and used as a representative scalar value. For each combination of (K_1, K_2) , the disentangled spectra A_i and B_i are computed iteratively (more details in [TS22](#)).

In case of our IFU observations of VFTS 812, the imperfect nebular line subtraction led to residuals in the sky-subtracted spectra that can considerably affect the disentangling and introduce artifacts in the disentangled spectra. To mitigate this effect, we change σ_i to a vector quantity $\sigma_{i,k}$ defined for all λ_k . We retain the continuum noise value for most wavelength bins, but arbitrarily increase $\sigma_{i,k}$ to 999 for $\lambda_k \in [4103.9, 4106.7] \text{ Å}$, which is affected by the nebular line as discussed in [Appendix B](#). With this modification, we can perform a meaningful spectral disentangling analysis despite residuals from sky subtraction.

Table D.1. Orbital elements for VFTS 812.

Parameter	Value
P [days]	17.28443 ± 0.00035
e	0.624 ± 0.009
ω [deg]	339.5 ± 1.3
$T_{0,\text{old}}$ [MJD]	54856.95 ± 0.04
$T_{0,\text{new}}$ [MJD]	60214.87 ± 0.04
$a \sin i [R_\odot]$	11.39 ± 0.25
$K_1 [\text{km s}^{-1}]$	42.7 ± 0.6

Appendix D.1: Input parameters

Spectral disentangling relies heavily on an accurate orbital solution; significant deviations from the same can easily introduce artificial features in the disentangled secondary spectrum. The orbital solution for VFTS 812 was first reported by [Almeida et al. \(2017\)](#) based on 32 epochs of observations covering the wavelength range 3964–4567 Å including several spectral lines. They only used He I and He II lines for RV measurement, since Balmer lines are typically broader and affected by nebular emission and wind effects ([Sana et al. 2013](#)). Our new observations in this work are limited to the H $_\delta$ line and are therefore not ideal to find a more constraining orbital solution than [Almeida et al. \(2017\)](#). Consequently, we adopt their solution in this work, with the only exception being time of periastron passage (T_0). With all other orbital elements fixed, we refit T_0 using the Spectroscopic and Interferometric Orbital Solution finer (spinOS) tool ([Fabry et al. 2021](#)) to update the ephemeris and ensure an accurate value for the new data. All orbital elements are summarized in [Table D.1](#).

Appendix D.2: Component flux ratios

For the injection study discussed in [Section 4.2](#), the mock data need to be synthesized using appropriate flux ratios between the primary and the injected secondary. Similar to [Shenar et al. \(2022a\)](#), we convolve our flux calibrated FASTWIND models with the Bessel B filter and take the ratio subsequently. [Table D.2](#) lists the computed flux ratios between different secondary models and the primary model.

Table D.2. Flux ratios for secondary models compared to the primary that were used in the injection study.

Secondary Mass [M_{\odot}]	Flux ratio [%]
5	1.1
5.5	1.3
6	1.6
6.5	1.9
7	2.3
8	3.1
10	5.1

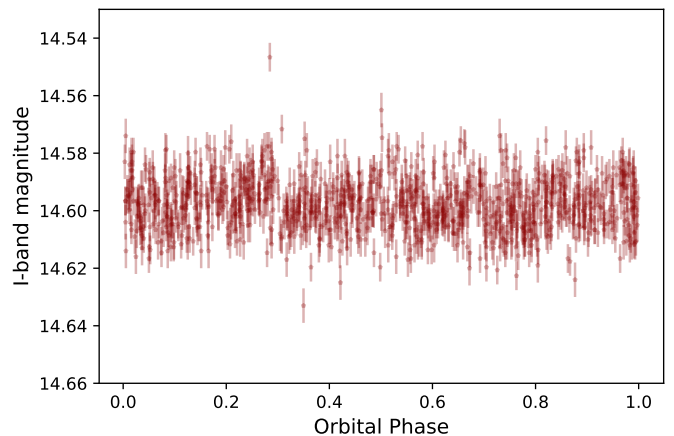


Fig. E.1. OGLE I-band light curve of VFTS 812, phase folded on the orbital period.

Appendix E: Photometric constraints

In Section 3.3, the lack of observed photometric variability in VFTS 812 was used to obtain an upper limit on the inclination, on the basis that a more edge-on orbit would produce an observable primary eclipse. Figure E.1 shows the OGLE I-band light curve that TS22 remarked on for not having any significant frequencies. Using a 3σ threshold, we find that the flux-dip from an eclipse has to be $> 2.6\%$ for detection. From spectral disentangling, we know that the flux contribution of the secondary is $\lesssim 1.6\%$ (see Sec. 4.2). A full eclipse of the primary by a $5.1 M_{\odot}$ companion with a radius of $\sim 2.3 R_{\odot}$ will cover $\sim 5\%$ of the primary surface, while contributing $\lesssim 1.6\%$ to the total flux, thus resulting in a flux-dip of $\gtrsim 3.4\%$. While partial eclipses can be considered for finer estimation of eclipse detectability, we adopt the full eclipse scenario to remain conservative. The lack of a detected eclipse therefore enables an additional inclination constraint on the MS companion scenario.

Furthermore, due to the geometry of the system, a stronger inclination constraint could in principle be obtained from the lack of an observed secondary eclipse. However, from spectral disentangling, the brightness of the companion is limited to $\lesssim 1.6\%$ that of the primary. A secondary eclipse should thus not be observable in OGLE data, and we did not consider this constraint further.

Similarly, the flatness of the light curve also indicates that there is no observed ellipsoidal variability in the primary. Ellipsoidal variability occurs when a star fills a significant fraction of its Roche lobe, thus the absence of such a feature (at fixed primary mass) provides a lower limit on the separation between the components at periastron, and an increase in the minimum secondary mass $M_{2,\min}$ relative to the unconstrained case. However, for an eccentric orbit, such an analysis requires detailed 3D modeling of the primary and its brightness fluctuations due to regular perturbations from the secondary near periastron. Such modeling was considered out of scope for this work, but may be relevant in future studies.